ELSEVIER

Journal of Neuroscience Methods 153 (2006) 221–229

JOURNAL OF NEUROSCIENCE METHODS

www.elsevier.com/locate/jneumeth

Compatibility of glass-guided recording microelectrodes in the brain stem of squirrel monkeys with high-resolution 3D MRI

R. Tammer [a,*], L. Ehrenreich [a], S. Boretius [b], T. Watanabe [b], J. Frahm [b], T. Michaelis [b]

[a] *Department of Neurobiology, Deutsches Primatenzentrum GmbH, Kellnerweg 4, 37077 Göttingen, Germany*
[b] *Biomedizinische NMR Forschungs GmbH am MPI für biophysikalische Chemie, 37070 Göttingen, Germany*

Received 6 July 2005; received in revised form 20 October 2005; accepted 31 October 2005

Abstract

Knowledge of the precise position of recording microelectrodes within the brain of a non-human primate is essential for a reliable exploration of very small anatomic structures. This work demonstrates the compatibility of a newly developed glass-guided microelectrode design and microfeed equipment with high-resolution 3D magnetic resonance imaging (MRI). T1- and T2-weighted images allow for the non-invasive visualization of chronically implanted microelectrodes within the brain stem of squirrel monkeys in vivo. Neural extracellular multi-unit recordings proved the functionality of the microelectrode before and after the use of 3D MRI suggesting the preservation of normal brain tissue at the tip of the electrode. Because histology confirmed the absence of lesions attributable to MRI, the approach offers an interactive monitoring during the course of neuroethological experiments. Consequently, MRI may become an in vivo alternative to common histological post mortem verifications of electrode tracks and hence may avoid the early sacrificing of primates after only a small number of experiments.

Keywords: 3D MRI; Primate; Chronic-implanted microelectrodes; Electrode compatibility; Telemetric electrophysiology

1. Introduction

Electrodes for brain stimulation or electrophysiological recordings need to be placed precisely in order to guarantee optimal results and efficient exploration — a prerequisite in research and therapeutic applications in animals as well as in humans. Neurobiological research in primates traditionally uses referential atlases to plan electrode positions and finally place electrodes with the aid of a stereotaxic apparatus. Exact positions of recording sites are commonly documented by histological brain sections stained with cresyl violet and chronic microelectrode tracks are visualized immunohistochemically using anti-glial fibrillary acidic protein (GFAP) antibody (Benevento and McCleary, 1992).

Due to its non-invasive nature, MRI has been applied to guide electrode placement in man and animals in vivo (Asahi et al., 2003; Duffner et al., 2002; Nahm et al., 1994; Saunders et al., 1990; Scherberger et al., 2003; Vayssiere et al., 2000). Some studies used MRI to detect metallic deposits at the exploration site in order to visualize tracks in the brain after removal of the electrodes (Fung et al., 1998; Pezaris and Dubowitz, 1999). Although MRI has been shown to verify lead locations of electrodes for deep brain stimulation (DBS) during post-surgical evaluation (Starr et al., 2002; Tronnier et al., 1999), the procedure may not be without risks for patients with brain stimulation devices (Rezai et al., 2004; Spiegel et al., 2003). In view of an increasing diagnostic demand, the reported health hazards related to MRI in conjunction with biomedical implants (implantable pulse generators and deep brain stimulators) raised human safety issues and prompted in vitro and in vivo studies that specifically address the full biocompatibility of combined procedures. Since primates, being phylogenetically at closest to man, are often used in research as systemic animal models to study either general biological principles such as vocalization and social behavior (Tammer et al., 2004) or human diseases (e.g., Parkinson disease, multiple sclerosis, Alzheimer disease), similar issues arise for MRI in primate research.

Among the plethora of investigated materials and devices are longitudinal metallic implants (Smith et al., 2000, 2001), in particular surgical clips (Davis et al., 1981), orthodontic materials (Planert et al., 1996), osteosynthetic plates (Buchli et al., 1988), stents and coils (Teitelbaum et al., 1988), biopsy

* Corresponding author. Tel.: +49 551 3851254; fax: +49 551 3851307.
E-mail address: rtammer@dpz.gwdg.de (R. Tammer).

0165-0270/$ – see front matter © 2005 Elsevier B.V. All rights reserved.
doi:10.1016/j.jneumeth.2005.10.018

needles and devices (Moscatel et al., 1995), medical instruments (Planert et al., 1996), cardiac pacemaker electrodes (Achenbach et al., 1997), endovascular guidewires (Konings et al., 2000) and catheters (Nitz et al., 2001), intravascular filters, neurosurgical implants (Shellock, 2001), non-ferrous noble metal electrodes (Bhavaraju et al., 2002), and neurostimulation systems (Rezai et al., 2002). The potential of MRI to cause lesions due to magnetic field interactions, induced electrical currents, thermal tissue damage, and disruption of operational aspects of these devices is stressed in studies of cardiac pacemakers (Pavlicek et al., 1983), implanted neurostimulators (Tronnier et al., 1999), stimulating leads implanted in deep brain areas (Starr et al., 2002), and of non-ferromagnetic surgical as well as dental materials and devices (New et al., 1983). Recently, Spiegel et al. (2003) and Rezai et al. (2004) described serious injuries and neurological symptoms in two patients with implanted deep brain devices, one with "externalized" not connected leads and the second with a bilateral implanted DBS system undergoing MRI. Nevertheless, the literature provides no satisfactory evidence that gives specific information for a safe application of MRI in monkeys with chronically implanted microelectrodes. Although in vitro and in vivo studies suggest reasonably safe MRI applications with implants, tissue damage might depend on the applied magnetic field strength, implanted material, its size, shape and position relative to the magnetic fields, and characteristics of the penetrated tissue (e.g., its blood perfusion). The purpose of this in vivo study was (i) to demonstrate the MRI compatibility of a glass-guided microelectrode design at 2.35 T, (ii) to visualize the position of the tip of the recording microelectrode relative to the target structure, and (iii) to verify by electrophysiological recordings and histological evaluations that the application of T1- and T2-weighted high-resolution 3D MRI does not induce lesions at the recording sites of implanted microelectrodes in the brain stem of primates.

2. Materials and methods

2.1. Experimental animals

Two adult squirrel monkeys (*Saimiri sciureus*) were implanted with a synthetic MRI-compatible platform designed to carry telemetric hardware. Both animals served in a neuroethological research project in order to investigate social vocal interaction of freely moving monkeys by telemetric electrophysiological neuronal recording. For the study presented here, both monkeys were implanted with newly developed glass-guided electrodes in order to assess their compatibility with MRI. After terminating the neuroethological experiments, the animals were sacrificed, perfused and brain stem sections were stained immunohistochemically for demonstration of electrode tracks. In addition, two adult female common marmoset monkeys (*Callithrix jacchus*) were implanted with a synthetic platform. In these animals, one set of glass-guided microelectrodes was placed before and a second set after MRI. The animals were sacrificed to identify "seats" of the microelectrode tips within brain tissue via hematoxylin–eosin histology. The animal experiments were approved by the Animal Ethics Committee of the District of Braunschweig, Government of Lower Saxony, Germany, reference no. 509.42502/08-10.03 and 509.42502/08-10.03 (E1).

2.2. Platform implantation in squirrel monkeys

The platform implantation procedure was carried out in general anesthesia using a mixture of 50 mg ketamine, 10 mg xylazine, and 0.1 mg atropine sulphate in 1 ml sterile water per kg body weight applied intramuscularly. After the surgical preparation, a circular full depth skin piece on the dome of the skull was removed. Four polyamide screws (Nylon®) were fitted through inverted T-shaped holes drilled into the skull bone. A dental acrylic cylinder was moulded directly onto the skull, thereby embedding and blocking the screws. A preformed, circular, dental acrylic (Paladur®, Merck, Germany) platform platelet (diameter 30 mm, height 4 mm) with a central round opening (inner diameter 9 mm) was glued onto the moulded cylinder. Routine wound closure with absorbable sutures (3/0 Vicryl®, Ethicon®, Johnson & Johnson, USA) was followed by post-surgical care consisting of buprenorphine (Temgesic®, Essex Pharma), 3 μg per kg body weight once a day (sid) for three consecutive days and antimicrobial treatment with enrofloxacine (Baytril®, Bayer, Germany) 10 mg per kg body weight sid for 1 week.

2.3. Glass-guided microelectrode and implantation technique

The microfeed was based on a custom-made precision potentiometer (19.05 mm × 4.83 mm × 6.35 mm, Vishay/Conrad, Germany) with all electrical parts removed (see Fig. 1). The spared epoxy case, the fine brass thread and tiny dental acrylic (Paladur®, Merck Germany) sledge (width 1–1.5 mm) moulded onto the thread bar, allowed forward/backward movement in a longitudinal, i.e. vertical direction by turning it with a screwdriver. The quartz glass-insulated platinum–tungsten (90%:10%) microelectrode (outer diameter (o.d.) 80 μm, electrical resistance 1 MΩ, metal core Ø 25 μm, Thomas Recording, Giessen, Germany) with pulled (o.d. ∼50 μm) and grinded tip was inserted into a "stabilizing" boro-silicate glass capillary (inner diameter (i.d.) 84 μm, o.d. 250 μm) and telescoped in a second, "guiding" boro-silicate glass capillary (i.d. 300 μm, o.d. 400 μm, Hilgenberg GmbH, Malsfeld, Germany). The cutting edge of the guiding tube's far end was melted and hence smoothened (rounded) (see Fig. 1C) by using an electrode puller's filament. A side effect of melting the end of a glass capillary is contraction of the lumen, centering and hence guidance of the microelectrode during advancement. We used a twin design with two guiding capillaries glued onto the far end of the epoxy base of the potentiometer with two components cement (Pattex Stabilit Express®, Henkel, Germany) before the telescoping stabilizing tubes with the fed in microelectrodes were inserted. After the metal core of the microelectrode was soldered to 50 mm long miniature braided Teflon®-coated stainless steel connection wire (7SS-2T, Science Products GmbH, Hofheim, Germany) with connectors, it was fixed onto the sledge together with the stabilizing tube using a drop of dental acrylic.

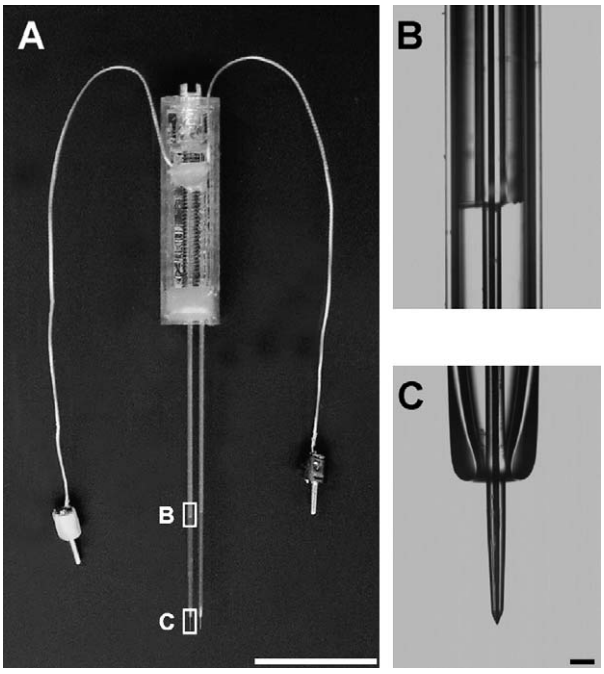

Fig. 1. (A) Macrophotograph of microfeed, consisting of modified potentiometer case, brass thread, attached glass capillary guided and stabilized microelectrodes, and braided connection wires with connectors. The white rectangles refer to the close-up views (B) and (C). Scale bar 1 cm. (B) Microphotograph of telescoping outer (guiding) and inner (stabilizing) glass capillary with microelectrode. (C) Outer glass capillary with melted and hence smoothened far end. Note that the microelectrode is directed by the narrowed orifice. Scale bar 100 μm.

The ground electrode consisted of a 0.16 mm × 30 mm sterile steel acupuncture needle (Seirin & Co., Shizuoka, Japan). It pierced through a separate hole at the caudal aspect of the platform to contact brain tissue. The microfeed (epoxy body and brass thread) remained affixed on the platform as well as the two connective wires (50 mm) solded to the electrode. The microfeed/microelectrode design applied to both species differed only in the length of the capillary which was up to 26 mm in the squirrel monkey and 14 mm in the common marmoset.

2.4. Platform and microelectrode implantation in common marmosets

In order to obtain comparative histological assessments, two adult female common marmosets were implanted with a dental acrylic platform (Ø 15 mm, thickness 4 mm) under general anesthesia using intramuscular injections of alfaxalonum 1.35 mg and alfadolon aceticum 0.45 mg per 100 Gramm body weight (Saffan®, Berna Veterinärprodukte AG), diazepam 0.125 mg (Valium®, Roche) and 0.5 mg atropine–sulphate per animal. In animal #1 one pair of electrodes was implanted into either brain hemisphere before MRI and a second pair after MRI. In animal #2 two pairs of electrodes were implanted into the left and right hemisphere before MRI and four additional pairs of electrodes after MRI. The latter electrodes served as controls for tissue trauma associated with the insertion of the microelectrode.

2.5. Animal fixation apparatus for squirrel monkeys and common marmosets

A home-made MR-compatible acrylic stereotaxic device was used to fixate the squirrel monkeys in a prone position (see Fig. 2). The body of the animal was placed in a half pipe (Scotchcast®, 3M, France) lined with a spiral PE-tubing creating a heating pad (surface temperature ∼35 °C) to support body temperature of the anesthetised animal. Respiration was monitored by a signal derived from a home-made pressure transducer fixed to the animal's chest. Fixation of common marmosets was accomplished by an animal fixation device similar to that for squirrel monkeys. The 5-point fixation principle (left and right lower orbital rim, counterfixating mouth bar and external ear canals) of the stereotaxic frame assembly (Model 1430 by David Kopf, USA) was scaled down to fit the size of the considerably smaller skulls of the common marmoset.

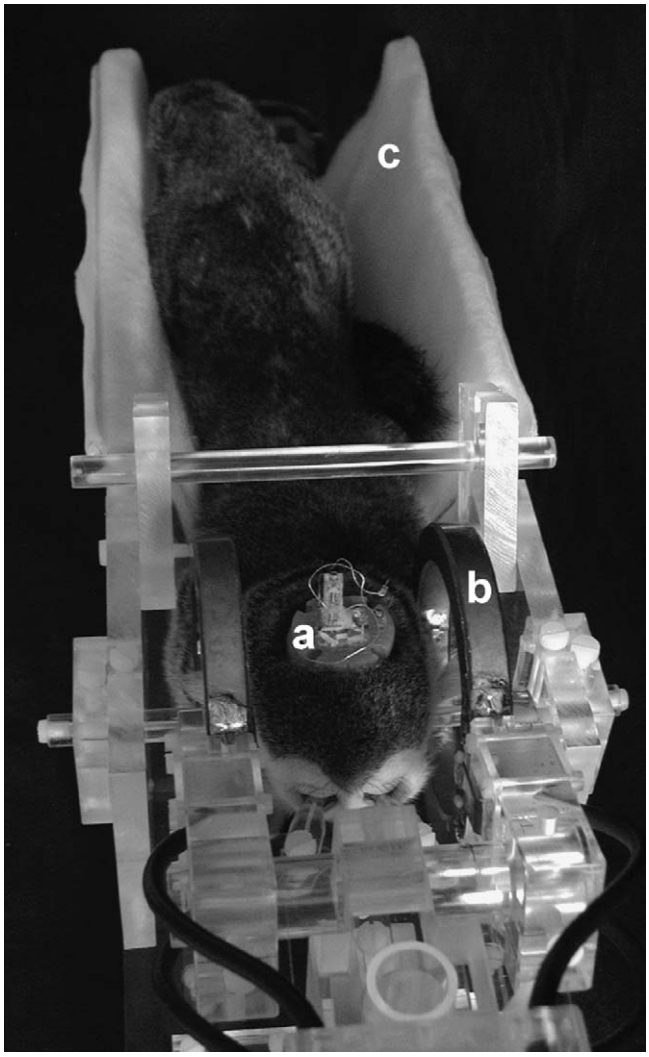

Fig. 2. Animal positioning and MRI coil setup. Squirrel monkeys (*Saimiri sciureus*) were examined in a prone position within the custom-made acrylic MR-compatible fixator a: synthetic, head-mounted platform with microfeed and implanted microelectrode, b: Helmholtz transmit/receive coil, o.d. 10 cm, c: warm water cushion lining the half pipe upholstered with hydrophobic cast bedding.

2.6. Magnetic resonance imaging in squirrel monkeys and common marmosets

High-resolution 3D MRI was carried out using T1-weighted (3D FLASH, TR/TE = 22.3/10.1 ms, isotropic resolution = 330 μm, two averages, 27 min) and T2-weighted sequences (3D FSE, TR/TE = 3000/127.3 ms, 16 echoes, echo-spacing = 16.1 ms, isotropic resolution = 469 μm, 51 min) at 2.35 T. The MRI system comprised a MRBR 4.7/400 mm magnet (Magnex Scientific, Abingdon, UK) equipped with B-GA20 gradients (i.d. 200 mm, 100 mT m^{-1}) driven by a DBX system (Bruker BioSpin MRI GmbH, Ettlingen, Germany). A home-made 100 mm Helmholtz radiofrequency coil was used in transmit/receive mode. The MRI parameters were identical in both species.

During MRI, squirrel monkeys were kept under general anaesthesia injecting a mixture of 25 mg ketamine, 5 mg xylazine and 0.05 mg atropine sulphate in 0.5 ml sterile water per kg body weight intramuscularly. Anesthesia was maintained, if necessary, with consecutive shots of half the dosage given after 45–60 min. After recovery the animals returned to their social group.

Common marmosets were premedicated and induced with the Saffan® anesthetic protocol, intubated with a 2/0 metric pediatric endotracheal tube (Portex®, Smith Medical International Ltd., UK) and kept under inhalation anesthesia using isoflurane (0.25%) with a carrier gas mixture of N_2O:O_2 (60:40%). After termination of the MRI examination, immobilization was sustained by administering a mixture of ketamine and xylazine following the anesthetic protocol used in squirrel monkeys.

2.7. Electrophysiology in the squirrel monkey

In squirrel monkey #1 a pair of microelectrodes was implanted directly above the caudal third of the right inferior colliculus and confirmed by MRI. The position of the tip of the electrode was kept at least 1 mm above the later recording site. Four weeks later the neuronal activity was recorded telemetrically while the animal was immobilised by injection anesthesia with a mixture of 25 mg ketamine, 5 mg xylazine, and 0.05 mg atropine sulphate in 0.5 ml sterile water per kg body weight applied intramuscularly. The head of the monkey was fixated in a horizontal position.

The neuronal activity was recorded by the telemetry technique developed by Grohrock et al. (1997). The microelectrodes were advanced manually by steps of 52 μm into a recording position at a height of the lower half of the inferior colliculus until multi-unit neuronal signals with a signal to noise ratio (SNR) of 2:1–3:1 in response to a 5 kHz sinus tone were detected. The sound was synthetically created by a sound designing program (Cool Edit 2000 Syntrillium Software Corporation, USA) and presented to the animal via two loudspeakers positioned on the left and right hand side of the monkey horizontally to and in 35 cm distance to its ears. Sound pressure level measured at the animal's auricles was about 80 dB. Neuronal activities and sounds were captured via Spike2 Software in conjunction with an analog/digital converting unit CED Micro1401 *mk*II interface (Cambridge Electronic Design Ltd., UK).

Once the multi-unit was recorded the animal was detached from its fixation and brought to the MRI site (5 min car drive). After T2-weighted 3D MRI the animal was transported back to the primate centre. The neuronal activity to the acoustic stimuli (5 kHz sinus tone) was again recorded, while the position of the microelectrodes remained unchanged. Subsequently, the procedure was repeated to obtain a T1-weighted 3D MRI data set followed by a third neuronal recording. The pair of electrodes applied for this study stayed in use. The animal recovered a few hours later and returned back into its social group. Five months later the animal was sacrificed.

2.8. Histology in the squirrel monkeys and common marmosets

All animals were perfused intracardially with saline (0.9% NaCl) followed by 4% buffered paraformaldehyde (PFA) while in deep general anaesthesia using a high dose of a mixture of ketamine and xylazine. Brains were extracted and stored at 4 °C in 4% PFA before treated with 20% saccharose solution for 3 days, frozen using liquid nitrogen, and stored at −60 °C.

Coronal brain sections (thickness 40 μm) of both squirrel monkeys were stained for GFAP (glial fibrillary acidic protein) to locate chronic electrode tracks using the method reported by Benevento and McCleary (1992). In the common marmosets, microelectrodes were retracted from their positions after intracardiac perfusion. Time lapse between implantation of electrodes and perfusion of the animals were 6 h (electrodes implanted before MRI) and 1–2 h (electrodes implanted after MRI), respectively. Coronal brain sections (thickness 10–15 μm) were stained with hematoxylin–eosin and searched for tissue lesions in sections tangential to electrode tracks.

3. Results and discussion

3.1. Magnetic resonance imaging in squirrel monkeys and common marmosets

Neither the parts of the dental acrylic platform nor the hardware of the recording device (epoxy potentiometer case with brass thread bar, dental acrylic sledge and braided, stainless steel connection wires with solded wrap connections) caused any visible magnetic susceptibility distortions in the obtained T2-weighted MR images (Fig. 3). The images revealed distinct anatomical details at 469 μm isotropic resolution but not the tip of the platinum–tungsten electrode. On the other hand, the two telescoped glass capillaries with the inserted quartz glass-insulated microelectrode and its metal core as well as the advanced microelectrode yielded mild susceptibility distortions in T1-weighted MR images, i.e. signal void on the order of 1–2 pixel around the microelectrodes. However, because of the much better isotropic resolution of 330 μm, T1-weighted images still allowed for a clear detection of the electrode tip within the brain stem (Fig. 3). Moreover, the tip position could be visualized at different extensions of the electrode (Fig. 4) and

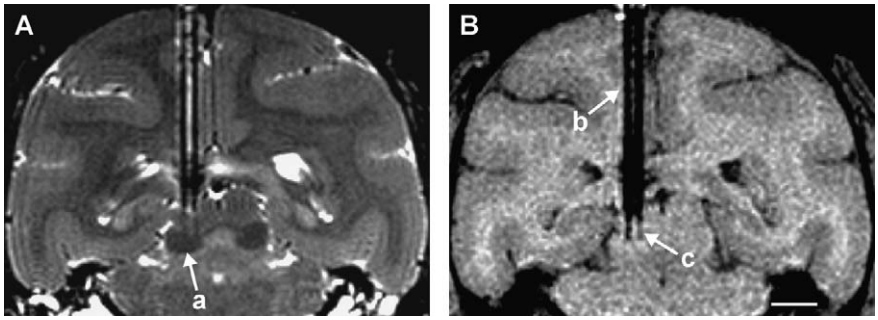

Fig. 3. (A) T2-weighted (469 μm isotropic resolution) and (B) T1-weighted 3D MRI (330 μm isotropic resolution) of the brain of squirrel monkey #1 with two inserted microelectrodes: (a) inferior colliculus, (b) telescoped glass capillaries with microelectrode platinum–tungsten core, (c) advanced microelectrode. Scale bar 5 mm.

assigned to the accordant anatomical anterior–posterior (A–P) plane depicted in Emmers and Akert (1963).

In agreement with the general findings reported by Uitti et al. (2002) for a 1.5 T MRI study of patients with Parkinson disease and DBS, the present data provided no evidence for a spatial deviation of the electrode position by more than one image voxel that is 330 μm. However, as a special case, Uitti et al. (2002) described one patient who showed a lateral deviation of up to 3 mm of a commercially available platinum–iridium DBS electrode (1 mm diameter) implanted into the thalamic and subthalamic nucleus.

The absence of major electrode movements is further supported by other animal studies. Jog et al. (2002) reported a tetrode assembly suitable for MRI electrode localization in rat brain using 2D multi-slice spin-echo MRI at 2.0 T. Coronal T1-weighted images allowed for A–P location of tetrodes (Ø 50 μm) which created a clear and distinct artefact of 180 μm. Assessment of tip height could be measured on sequential transverse T1-weighted sections with a margin of error of 180 μm. T2-weighted images enhanced gray–white differentiation of brain tissue but blurred the nickel–chromium electrode tip position due to signal loss. This is in line with our experience, if T2-weighted MRI is used to visualize platinum–tungsten electrodes. The authors reported no loss of neuronal activity or the occurrence of tissue lesions due to the exposure of the electrodes to the MRI examination. Drifts in neuronal recording were apparently caused by relaxing tissue movement after the electrode was advanced or due to respiration-induced changes in brain volume and did not interfere with cluster identification. Similarly, Sheliga et al. (1999) identified electrode locations in the brain of rhesus monkey in vivo using MRI at 1.5 T. They inserted 120 μm tungsten wires as "markers" 3–5 mm above the positions of 80 μm tungsten recording electrodes and reported no significant distortion of the surrounding brain tissue around the marker wires.

3.2. Electrophysiology in the squirrel monkey

Neuronal multi-unit electrophysiological activity from the right inferior colliculus of squirrel monkey #1 could be recorded via telemetry on each of the two inserted microelectrodes (Fig. 5). Throughout all recordings neuronal activity was strictly correlated and exclusively linked to the presented stimulus. The first of the three consecutive recordings from the first multi-unit (N1) before T2-weighted 3D MRI showed a clear and stable neuronal signal with a signal-to-noise ratio (SNR) of about 2:1 and an initial burst of higher frequency of electric activity as a result of the start of the auditory stimulus (see Fig. 5, time 0:00 [h:min]). The neuronal activity recorded from the second multi-unit (N2) reached a SNR of about 3:1, although the majority of neurons lay within a SNR of 2:1. After T2-weighted 3D MRI no qualitative change of N1 in respect to SNR or absolute spike height was demonstrable, whereas the recorded trace of N2 (see Fig. 5, time 2:17 [h:min]) showed a higher SNR of 4:1, even reaching a SNR of 5:1 in single spikes. SNR was slightly decreased, but stimulus correlated multi-unit activity was clearly preserved. In contrast to N1, the height of single spikes of N2 peaked with a SNR of 5:1. In the third recording, taken after

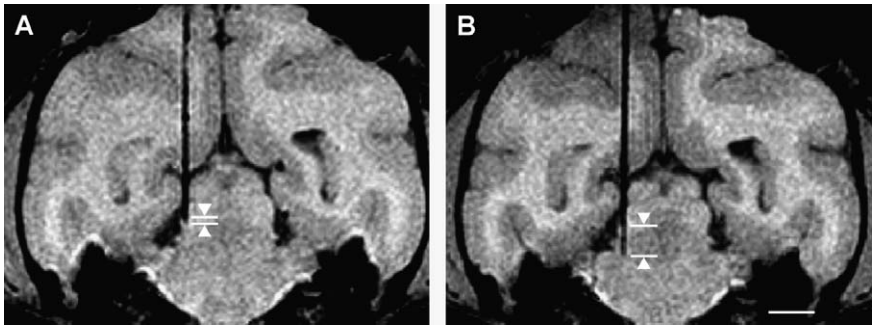

Fig. 4. T1-weighted 3D MRI (330 μm isotropic resolution) of the brain of squirrel monkey #1 demonstrating a single microelectrode within telescoped glass capillaries. Two different extensions of (A) 0.4 mm and (B) 2.9 mm, measured from glass capillary end to electrode tip, are depicted by white arrows. Scale bar 5 mm.

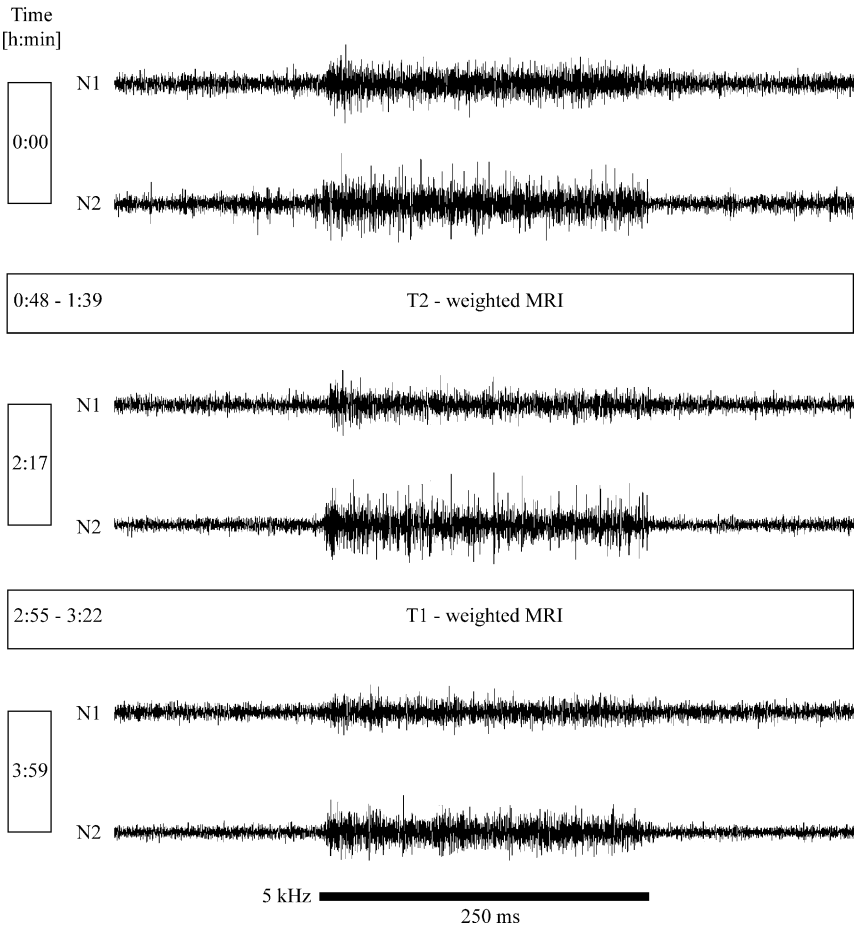

Fig. 5. Neuronal traces (N1 and N2) from two auditory neuronal multi-units in the right inferior colliculus of squirrel monkey #1 before MRI (at 0:00), after T2-weighted 3D MRI (at 2 h 17 min), and after T1-weighted 3D MRI (at 3 h 59 min). The traces were recorded simultaneously by a pair of microelectrodes (see Fig. 1A) and transmitted telemetrically via two head-mounted miniature transmitters. The scale bar indicates the duration of the auditory stimuli (5 kHz sinus tone). Note the synchronous neuronal activity in all traces.

T1-weighted 3D MRI (see Fig. 5, time 3:59 [h:min]), N1 lost signal density of the firing multi-unit, although single spikes still reflected neuronal activity with a SNR of 2:1. N2 activity decreased to a SNR of 3:1. Although an overall loss of signal (lowered SNR) was detectable over the experimental period of about 4 h, the recording of the stimulated multi-unit remained significant for analysis.

In general, the electrophysiological results indicate that the chosen MRI procedures did not distinctively alter or abolish extracellular multi-unit recordings. As the neurophysiological behavior of single neurons with respect to spike shape or firing rate was not examined, the observed modulation of the neuronal activity pattern of the recorded multi-unit cell assembly might reflect minor movements of the electrode tip relative to the target tissue due to MRI, transport of the animal, or physiological movements/volume changes of the brain (blood pressure, pulse rate, respiration). In addition to respiration-induced changes in brain volume, Jog et al. (2002) reported major signal peak drifts as a result of tissue movement after advancement of the electrode. In line with our findings, respective drifts were noticeable but did not interfere with the ability to reliably identify clusters. Here, changes in the recorded neuronal activity of auditory multi-units were obvious but did not conceal the clear synchronous correlation of activity stimulated by a 5 kHz sinus tone stimulus.

3.3. Histology in squirrel monkeys

After termination of the neuroethological experiment animals were sacrificed. Fig. 6 compares an electrode track of animal #2 as seen by T1-weighted 3D MRI in a coronal section of the brain stem in vivo with a histological section obtained several months later. Although MRI lacks anatomical detail, reference to a stereotaxic atlas allows for reasonable verification of the electrode position. The GFAP-stained section depicts the electrode ending in the fibre bundle of the lateral lemniscus. It is in general agreement with the MRI finding in spite of a 22% shrinkage of the brain tissue due to preparation. For visual inspection both images have been scaled accordingly.

3.4. Histology in common marmosets

Despite extensive histological preparation and search of cut sections perpendicular to the electrode tracks, the centre cut of

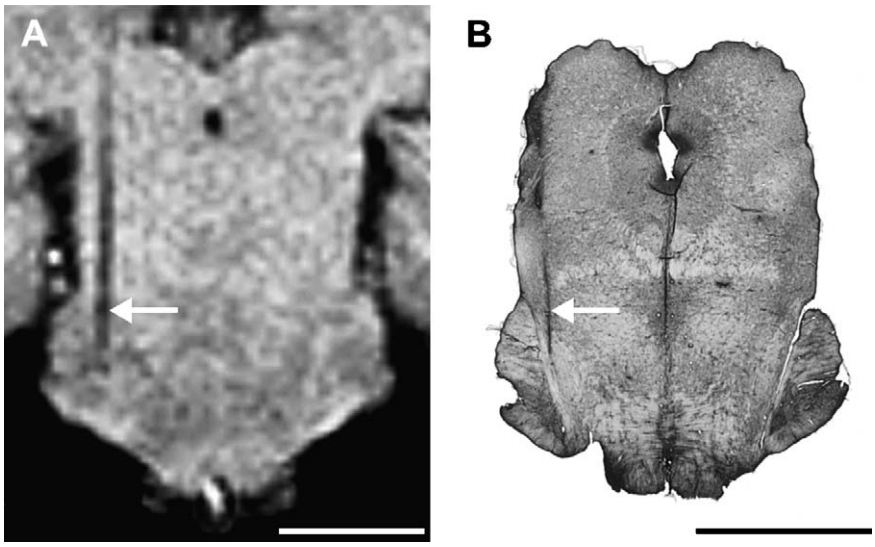

Fig. 6. (A) T1-weighted 3D MRI (330 μm isotropic resolution) of the brain stem of squirrel monkey #2 demonstrating the microelectrode and its tip (white arrow) at exploration endpoint during the phase of the neuroethological experiments. Scale bar 5 mm. (B) Glial fibrillary acidic protein (GFAP)-stained coronal section (thickness 40 μm) of the same monkey obtained several months later. Please note the shrinkage of the histological specimen relative to the size of the brain stem as given by MRI. Scale bar 5 mm.

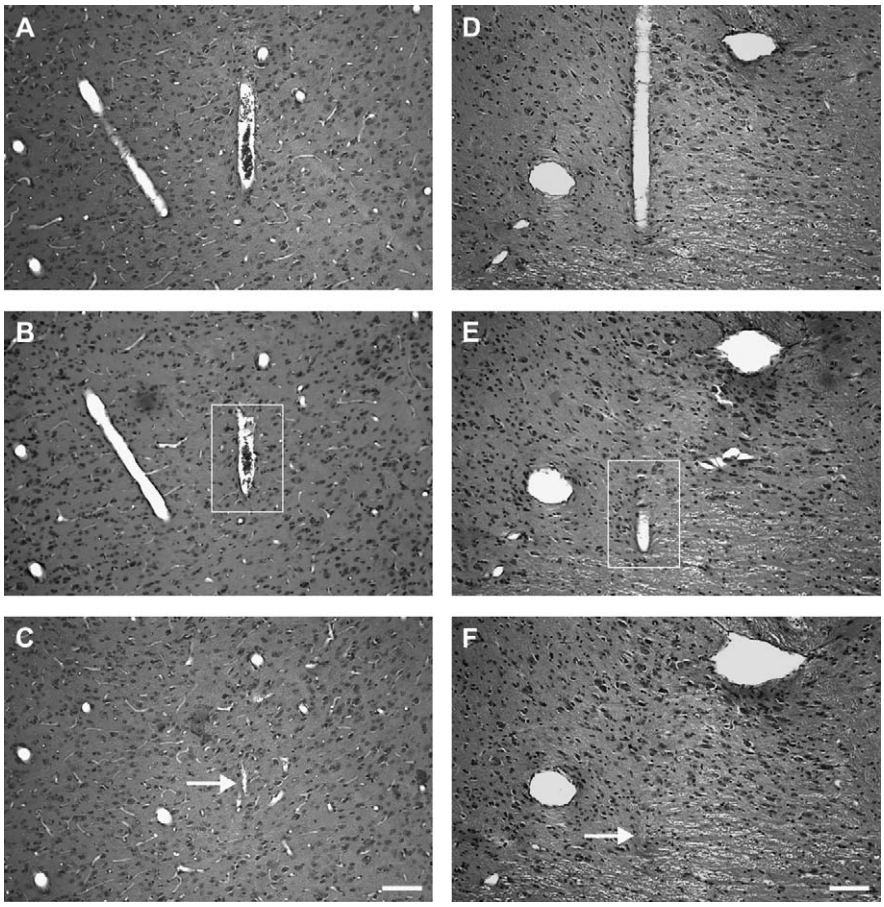

Fig. 7. Hematoxylin–eosin stains (thickness 10–15 μm) of the brain of common marmoset monkeys (*Callithrix jacchus*) depicting three consecutive sections of a microelectrode track (A–C) without MRI exposure (animal #1) and (D–F) after MRI (animal #2). Please note the different cell density of A–C compared to D–F which is due to different brain regions hit by the electrodes. Magnified views of the electrode "seats" (white rectangles) are shown in Fig. 8. Scale bars 100 μm.

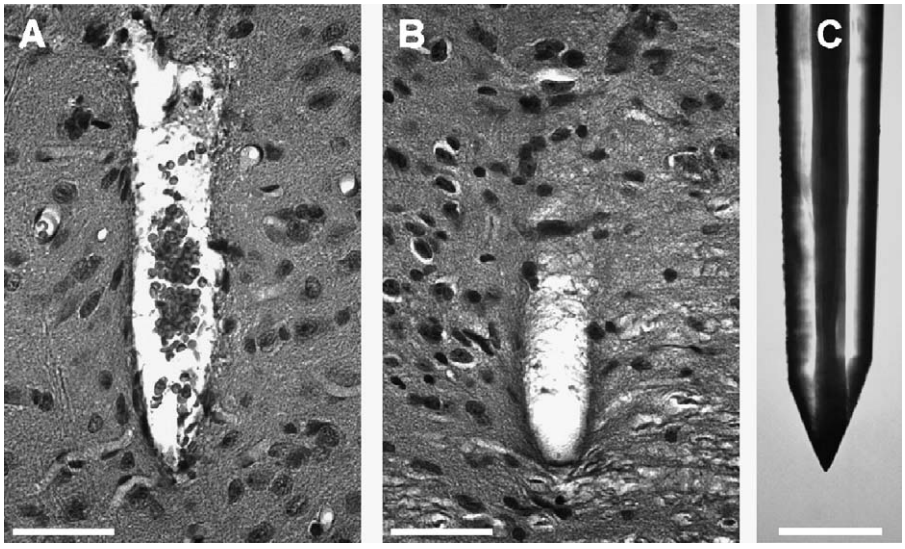

Fig. 8. Magnified views of hematoxylin–eosin stains (thickness 10–15 μm) of the brain of common marmosets depicting longitudinal (tangential) sections of two microelectrode tracks of (A) without MRI exposure (animal #1) and (B) after MRI (animal #2). The latter track lies close to a fibre rich brain region. (C) Microphotograph of the grinded tip of a quartz glass coated platinum–tungsten microelectrode. Scale bars 50 μm.

an electrode tip's "seat" within the tissue could not be reliably identified except for two histological specimens on tangential sections. Tracks were clearly identified by centrally coagulated hemorrhages, fibrin deposits, perifocal spongiform loosening of neuropil, and astrocytic edema as a result of tissue trauma. Comparative histological evaluation of tissue lesions by light microscopy of hematoxylin–eosin-stained longitudinal sections showed no specific tissue damage caused by MRI (Figs. 7 and 8). The microelectrodes implanted before MRI resulted in similar tissue lesions to those implanted after MRI. Detectable lesions were caused by simple mechanical trauma from displacement and disruption of the cellular network due to the insertion of the glass-guided microelectrodes and equivalent to lesions caused by steel-guided electrodes.

In this study histological sections of the "seat" of the electrode within the tissue suggests no or only very little movement of the tip and no detectable cell damage due to friction, movement, or MRI-induced tissue heating. Energy deposition in the tissue due to alternating magnetic fields and the presence of conductive (metallic) bodies such as microelectrodes or intravascular catheters should be expected to occur within minutes after MRI. Using T1-weighted spin-echo MRI at 1.5 T Achenbach et al. (1997) reported increased tissue temperatures of up to 90 °C at the tip of cardiac pacemaker electrodes (overall length ~60 cm) which must be considered potent enough to cause thermal necrosis. However, neither the length (600 mm versus 25 mm) nor the shape (circular/spiral versus linear) of the electrodes were comparable to the present study. Moreover, the recording microelectrode itself is insulated by quartz glass and is further wrapped up in the guiding glass capillary, so that a considerable temperature rise along the shaft would be necessary to damage surrounding tissue. Although it cannot be entirely excluded that mechanical tissue disruption along the track potentially conceals heat-induced cell death, any heating damage would be expected to be most pronounced at the end or tip of a metallic body and not equally distributed along the device. In the present study, the microelectrode tip displaced the surrounding tissue with only very minor disruption, so that masking of spherical necroses due to radiating heat may be excluded. Taken into account that potential heat damage is a function of the size, shape, and material of the microelectrode or lead, the present results hint to an ideal configuration of our particular experimental setup. Nevertheless, a potentially delayed stimulation of glial cell proliferation, detectable only after a few days, was not subject of this investigation. In fact, because gliosis seems an inevitable event of electrode insertion alone (Marín et al., 2005), this study focused on the neuronal activity close to the tip of a recording electrode as an indicator of a putative direct effect of MRI on vital cell function.

4. Conclusions

The newly developed setup of a custom-made microfeed, attached to a pair of glass capillary, for guiding commercially available platinum–tungsten microelectrodes was demonstrated to be fully MRI-compatible. Electrophysiological testing and histological evaluation of microelectrode tip implantation sites did not reveal tissue lesions associated with MRI investigations. The reported results prove high-resolution 3D MRI to be useful for verification of microelectrodes and hence interactive monitoring microelectrode positions in vivo. This technique potentially substitutes for post mortem electrode track verification by histology and can be applied in specific experimental designs where the sacrifice of an experimental animal is not an option. It might therefore add considerably to laboratory primate welfare and, in a similar manner, improve comparable applications in other laboratory animals.

Acknowledgements

We thank Prof. U. Jürgens for kindly supporting the project as well as Prof. F.J. Kaup, N. Knöchelmann, and K. Jarry for histopathological analyses (all Deutsches Primatenzentrum GmbH).

References

Achenbach S, Moshage W, Diem B, Bieberle T, Schibgilla V, Bachmann K. Effects of magnetic resonance imaging on cardiac pacemakers and electrodes. Am Heart J 1997;134:467–73.

Asahi T, Tamura R, Eifuku S, Hayashi N, Endo S, Nishijo H, et al. A method for accurate determination of stereotaxic coordinates in single-unit recording studies in monkeys by high-resolution three-dimensional magnetic resonance imaging. Neurosci Res 2003;47:255–60.

Benevento LA, McCleary LB. An immunohistochemical method for marking microelectrode tracks following single-unit recordings in long surviving, awake monkeys. J Neurosci Methods 1992;41:199–204.

Bhavaraju NC, Nagaraddi V, Chetlapalli SR, Osorio I. Electrical and thermal behavior of non-ferrous noble metal electrodes exposed to MRI fields. Magn Reson Imaging 2002;20:351–7.

Buchli R, Boesiger P, Meier D. Heating of metallic implants by MRI examinations. Magn Reson Med 1988;7:255–61.

Davis PL, Crooks L, Arakawa M, McRee R, Kaufman L, Margulis AR. Potential hazards in NMR imaging: heating effects of changing magnetic fields and RF fields on small metallic implants. AJR Am J Roentgenol 1981;137:857–60.

Duffner F, Schiffbauer H, Breit S, Friese S, Freudenstein D. Relevance of image fusion for target point determination in functional neurosurgery. Acta Neurochir 2002;144:445–51.

Emmers R, Akert K. A stereotaxic atlas of the brain of the squirrel monkey (*Saimiri sciureus*). Madison: The University of Wisconsin Press; 1963.

Fung SH, Burstein D, Born RT. In vivo microelectrode track reconstruction using magnetic resonance imaging. J Neurosci Methods 1998;80:215–24.

Grohrock P, Häusler U, Jürgens U. Dual-channel telemetry system for recording vocalization-correlated neuronal activity in freely moving squirrel monkeys. J Neurosci Methods 1997;76:7–13.

Jog MS, Conolly CI, Kubota Y, Iyengar DR, Garrido L, Harlan R, et al. Tetrode technology: advances, and data analysis techniques. J Neurosci Methods 2002;117:141–52.

Konings MK, Bartels LW, Smits H, Bakker C. Heating around intravascular guidewires by resonating RF waves. J Magn Reson Imaging 2000;12:79–85.

Marín C, Sales J, Botella C, Aranda I, McDermott R, Norman R, et al. Cellular response to implantation of penetrating intracortical microelectrode arrays into cerebral cortex. In: Zimmermann H, Krieglstein K, editors. Proceedings of 30th Göttingen Neurobiology Conference; 2005. p. 834.

Moscatel MA, Shellock FG, Morisoli SM. Biopsy needles and devices: assessment of ferromagnetism and artefacts during exposure to a 1.5 T MR System. J Magn Reson Imaging 1995;5:369–72.

Nahm FKD, Dale AM, Albright TD, Amaral DG. In vivo microelectrode localization in the brain of the alert monkey: a combined radiographic and magnetic resonance imaging approach. Exp Brain Res 1994;98:401–11.

New PFJ, Rosen BR, Brady TJ, Buonanno FS, Kistler JP, Burt CT, et al. Potential hazards and artefacts of ferromagnetic and nonferromagnetic surgical and dental materials and devices in nuclear magnetic resonance imaging. Radiology 1983;147:139–48.

Nitz WR, Oppelt A, Renz W, Manke C, Lenhart M, Link J. On the heating of linear conductive structures as guide wires and catheters in interventional MRI. J Magn Reson Imaging 2001;13:105–14.

Pavlicek W, Geisinger M, Castle L, Borkowski G, Meaney TF, Bream BL, et al. The effects of nuclear magnetic resonance on patients with cardiac pacemakers. Radiology 1983;147:149–53.

Pezaris JS, Dubowitz DJ. MRI localization of extracellular electrodes using metallic deposition at 1.5 T. Proc Intl Soc Mag Reson Med 1999;7:968.

Planert J, Modler H, Vosshenrich R. Measurements of magnetism-related forces and torque moments affecting medical instruments, implants, and foreign objects during magnetic resonance imaging at all degrees of freedom. Med Phys 1996;23:851–6.

Rezai A, Finelli D, Nyenhuis JA, Hrdlicka G, Tkach J, Sharan A, et al. Neurostimulation systems for deep brain stimulation: in vitro evaluation of magnetic resonance imaging-related heating at 1.5 T. J Magn Reson Imaging 2002;15:241–50.

Rezai A, Phillips M, Baker KB, Sharan AD, Nyenhuis J, Tkach J, et al. Neurostimulation system used for deep brain stimulation (DBS): MR safety issues and implications of failing to follow safety recommendations. Invest Radiol 2004;39:300–3.

Saunders RC, Aigner TG, Frank JA. Magnetic resonance imaging of the rhesus monkey brain: use for stereotactic neurosurgery. Exp Brain Res 1990;81:443–6.

Scherberger H, Fineman I, Musallam S, Dubowitz DJ, Bernheim KA, Pesaran B, et al. Magnetic resonance image-guided implantation of chronic recording electrodes in the macaque intraparietal sulcus. J Neurosci Methods 2003;130:1–8.

Sheliga BM, Yakushin SB, Silvers A, Raphan T, Cohen B. Control of spatial orientation of the angular vestibulo-ocular reflex by the nodulus and uvula of the vestibulocerebellum. Ann NY Acad Sci 1999;871:94–122.

Shellock FG. Metallic neurosurgical implants: evaluation of magnetic field interactions, heating, and artefacts at 1.5-Tesla. J Magn Reson Imaging 2001;14:295–9.

Smith CD, Kildishev AV, Nyenhuis JA, Foster KS, Bourland JD. Interactions of magnetic resonance imaging radio frequency magnetic fields with elongated medical implants. J Appl Phys 2000;87:6188–90.

Smith CD, Nyenhuis JA, Kildishev AV. Health effects of induced electric fields: implications for metallic implants. In: Shellock FG, editor. Magnetic resonance: health effects and safety, 16. Boca Raton, FL: CRC Press; 2001. p. 393–413.

Spiegel J, Fuss G, Backens M, Reith W, Magnus T, Becker G, et al. Transient dystonia following magnetic resonance imaging in a patient with deep brain stimulation electrodes for the treatment of Parkinson disease. Case report. J Neurosurg 2003;99:772–4.

Starr PA, Christine CW, Theodosopoulos PV, Lindsey N, Byrd D, Mosley A, et al. Implantation of deep brain stimulators into the subthalamic nucleus: technical approach and magnetic resonance imaging-verified lead locations. J Neurosurg 2002;97:370–87.

Tammer R, Ehrenreich L, Jürgens U. Telemetrically recorded neuronal activity in the inferior colliculus and bordering tegmentum during vocal communication in squirrel monkeys (*Saimiri sciureus*). Behav Brain Res 2004;151:331–6.

Teitelbaum GP, Bradley WG, Klein BD. MR imaging artifacts, ferromagnetism, and magnetic torque of intravascular filters, stents, and coils. Radiology 1988;166:657–64.

Tronnier VM, Staubert A, Hähnel S, Sarem-Aslani A. Magnetic resonance imaging with implanted neurostimulators: an in vitro and in vivo study. Neurosurgery 1999;44:118–25.

Uitti RJ, Tsuboi Y, Pooley RA, Putzke JD, Turk MF, Wszolek ZK, et al. Magnetic resonance imaging and deep brain stimulation. Neurosurgery 2002;51:1423–8.

Vayssiere N, Hemm S, Zanca M, Picot MC, Bonafe A, Cif L, et al. Magnetic resonance imaging stereotactic target localization for deep brain stimulation in dystonic children. J Neurosurg 2000;93:784–90.